crystals

MDPI

Article

High-Resolution X-Ray Imaging Using $Cs_3Cu_2Br_{1.25}I_{3.75}$ Scintillator Arrays Grown by In Situ Solution Processing

Xinlin Li [1,2], Zhenxin Yan [1,2], Baoyu Zhou [1,2], Junhua Hu [1,2], Ziyu Zhao [1,2] and Tao Lin [1,2,*]

[1] School of Physical Science and Technology, Laboratory of Optoelectronic Materials and Detection Technology, Guangxi Key Laboratory for Relativistic Astrophysics, Guangxi University, Nanning 530004, China; lixinlin@st.gxu.edu.cn (X.L.); yanzhenxin81@163.com (Z.Y.); zhoubaoyu20031@outlook.com (B.Z.); gxujunhua@163.com (J.H.); zhaoziyu20021@163.com (Z.Z.)

[2] Center on Nanoenergy Research, Guangxi University, Nanning 530004, China

* Correspondence: taolin@gxu.edu.cn

Abstract

Low-dimensional lead-free metal halide perovskites have demonstrated excellent performance in indirect X-ray detectors; however, the imaging resolution remains limited due to the lack of effective scintillation waveguiding. In this work, array-structured scintillation screens were fabricated using anodic aluminum oxide (AAO) templates via a spatial confinement–assisted in situ growth strategy. The resulting directional optical confinement effect significantly enhances the scintillation performance of the screen. The fabricated $Cs_3Cu_2Br_{1.25}I_{3.75}$-AAO scintillator arrays achieve a spatial resolution of 14.10 lp/mm and a minimum detectable dose rate of 243 nGy/s under X-ray irradiation. In addition, the scintillator arrays exhibit excellent radiation stability, providing a reliable and cost-effective solution for high-resolution array-based X-ray imaging.

Keywords: X-ray imaging; scintillator; waveguiding effect

1. Introduction

X-ray detection plays a crucial role in a wide range of applications, including medical imaging, nondestructive testing, security inspection, and industrial monitoring [1–7]. Among the available detection technologies, indirect X-ray detectors represent the predominant approach. In these systems, scintillators convert invisible high-energy X-ray photons into low-energy visible light, which is then collected by highly sensitive photodetectors to achieve efficient X-ray detection and energy discrimination [8–12]. Owing to their relatively simple system configuration, high operational stability, and controllable fabrication cost, indirect X-ray detectors have been widely adopted in both scientific research and practical applications. As the key functional component of indirect X-ray detectors, scintillator materials play a decisive role in determining imaging sensitivity, spatial resolution, and energy response characteristics. Their optical properties, structural morphology, and process controllability directly affect overall imaging performance. In recent years, metal halide perovskite materials have attracted increasing attention in the field of X-ray scintillation and have emerged as an important class of high-performance imaging materials [5,13–19]. These materials exhibit several intrinsic advantages, including high X-ray absorption cross sections, excellent photoluminescence quantum yields (PLQY), tunable band gaps, short decay lifetimes, and good solution processability. As a result, metal halide perovskites show considerable potential for improving imaging sensitivity, signal-to-noise ratio, and

Academic Editors: Stratos David and Luigi Montalto

Received: 27 January 2026
Revised: 2 February 2026
Accepted: 4 February 2026
Published: 7 February 2026

compatibility with various device architectures. At the material level, the scintillation performance of metal halide perovskites can be effectively tuned through halide-composition engineering. Therefore, mixed-halide systems have been demonstrated to be a practical and effective route to optimize scintillation efficiency and material stability [20–22].

Despite these advantages, conventional perovskite scintillation screens are typically fabricated as polycrystalline thick films [17,23]. In such structures, scintillation photons undergo significant scattering at grain boundaries and internal interfaces, leading to pronounced optical diffusion. This diffusion effect results in inter-pixel signal crosstalk, which limits further improvement in spatial resolution and ultimately causes blurred image edges and loss of fine structural details. Therefore, overcoming photon scattering and suppressing optical crosstalk remain critical challenges for achieving high-resolution perovskite-based X-ray imaging. To address these limitations, the construction of arrayed scintillator architectures with optical waveguiding effects has been widely explored. For example, Rocha et al. [24] fabricated regular patterned arrays on silicon substrates using conventional photolithography, followed by solution-based deposition and crystallization of perovskite precursors within predefined regions, resulting in arrayed scintillators with improved spatial resolution. Cha et al. [25] employed deep reactive ion etching (DRIE) to create high-aspect-ratio microhole structures in silicon substrates, which were subsequently filled with perovskite precursor solutions to enable in situ crystallization. The resulting arrays exhibited effective optical confinement and reduced inter-pixel crosstalk. Shao et al. [26] utilized three-dimensional printing to fabricate periodic groove structures, followed by aluminum deposition and recrystallization of perovskite crystals within the microstructures. In this configuration, scintillation photons propagated preferentially along the grooves and were confined within individual pixels by the reflective aluminum layer. In addition, Wang et al. [27] controlled the directional growth of perovskite single crystals by introducing hydrophilic and hydrophobic printed substrates, successfully achieving oriented $MAPbCl_3$ single-crystal arrays on solid substrates. This strategy was also demonstrated to be applicable to various perovskite compositions, such as $MAPbBr_3$, $CsPbCl_3$, and $CsPbBr_3$. Although these approaches effectively improve spatial resolution through structural design, most reported methods rely on complex microfabrication techniques or multistep processing procedures. Such complexity increases fabrication cost and may introduce risks of structural damage or material aggregation during scintillator preparation. Therefore, there is still a strong need for an efficient, low-cost, and facile strategy to fabricate high-resolution arrayed scintillator screens with good structural uniformity and reproducibility.

In this work, anodic aluminum oxide (AAO) with nanoscale pore dimensions is employed as a template for array construction. The AAO template features highly ordered pore arrangements with uniform pore size, good structural homogeneity, mature fabrication processes, and relatively low cost. Moreover, Al_2O_3 is nearly transparent to X-rays, thereby minimizing additional absorption losses during detection [28]. To achieve a balanced combination of scintillation efficiency and material stability, a mixed-halide copper halide perovskite composition, $Cs_3Cu_2Br_{1.25}I_{3.75}$, was selected by leveraging the complementary characteristics of Br- and I-containing end-member systems (i.e., Br-rich compositions typically exhibit improved stability [29], whereas I-rich compositions often show higher luminescence efficiency [30]). A spatially confined evaporation-assisted crystallization strategy is then adopted to achieve in situ growth of $Cs_3Cu_2Br_{1.25}I_{3.75}$ single crystals within the AAO nanopores, resulting in a $Cs_3Cu_2Br_{1.25}I_{3.75}$-AAO scintillator array. Under X-ray excitation, the fabricated array exhibits intense blue emission with a PLQY of 62% and a photoluminescence lifetime of 1.93 μs, together with good moisture, oxygen, and radiation stability. Benefiting from effective longitudinal optical confinement and lateral optical

isolation between adjacent pixels, the scintillator array achieves a spatial resolution of 14.10 lp/mm and a low detection limit of 243 nGy/s in practical imaging tests, demonstrating its strong potential for high-resolution, low-dose X-ray imaging applications.

2. Materials and Methods

2.1. Materials

Cesium carbonate (Cs_2CO_3, 99.5%), cesium bromide (CsBr, 99.9%), cesium iodide (CsI, 99.9%), and N,N-dimethylformamide (DMF, 99.9%) were purchased from Aladdin Biochemical Technology Co., Ltd. (Shanghai, China). Hydroiodic acid (HI, 55–58%), cuprous iodide (CuI, 99%), poly (methyl methacrylate) (PMMA, 99%), and dimethyl sulfoxide (DMSO, 99%) were obtained from Macklin Biochemical Co., Ltd. (Shanghai, China).

2.2. Synthesis Methods of $Cs_3Cu_2Br_{1.25}I_{3.75}$ Crystal Powder

In this work, $Cs_3Cu_2Br_{1.25}I_{3.75}$ crystal powder was prepared using a liquid-phase cooling crystallization method. Specifically, 3.5 mmol of Cs_2CO_3, 5 mmol of CsBr, and 8 mmol of CuI were added to 3 mL of hydroiodic acid (HI). The mixture was heated to 130 °C under stirring until a clear solution was obtained, followed by natural and slow cooling to room temperature. Upon cooling to room temperature, $Cs_3Cu_2Br_{1.25}I_{3.75}$ crystals precipitated from the solution. The crystals were separated from the precursor solution, washed with anhydrous isopropanol, and then separated from the solvent. Finally, the obtained $Cs_3Cu_2Br_{1.25}I_{3.75}$ crystal powder was dried for further use. Throughout this work, the material is referred to as $Cs_3Cu_2Br_{1.25}I_{3.75}$ based on the nominal precursor stoichiometry and the agreement of the XRD patterns with reported literature [20].

2.3. Synthesis Methods of $Cs_3Cu_2Br_{1.25}I_{3.75}$-Film Scintillation Screen

$Cs_3Cu_2Br_{1.25}I_{3.75}$-Film was prepared using the following procedure. Initially, 0.4 g of poly (methyl methacrylate) (PMMA) was dissolved in 1 mL of toluene under continuous stirring at 100 °C until complete dissolution occurred, after which the solution was cooled and maintained at 60 °C. Concurrently, single crystals of $Cs_3Cu_2Br_{1.25}I_{3.75}$ were thoroughly ground in a quartz mortar for approximately 20 min, yielding a homogeneous, finely powdered material. Subsequently, 0.1 g of the obtained $Cs_3Cu_2Br_{1.25}I_{3.75}$ crystalline powder was introduced into the PMMA solution and stirred continuously for an additional 30 min to ensure uniform dispersion. The resulting mixture was then cast into a circular mold (diameter: 2 cm), and the solvent was allowed to evaporate naturally at room temperature in air for 12 h.

2.4. Synthesis Methods of $Cs_3Cu_2Br_{1.25}I_{3.75}$-AAO Scintillation Screen

First, 0.7 mmol of CsI, 0.8 mmol of CuI, and 0.5 mmol of CsBr were dissolved in a mixed solvent consisting of 0.84 mL of dimethyl sulfoxide (DMSO) and 0.36 mL of N, N-dimethylformamide (DMF). The solution was stirred at 100 °C until a clear and transparent precursor solution was obtained. The precursor solution was then filtered using a syringe filter with a pore size of 0.22 μm. The AAO templates were sequentially ultrasonically cleaned in deionized water and ethanol for 5 min each, followed by drying under a nitrogen flow. Subsequently, 200 μL of the precursor solution was dropped onto the surface of a cleaned AAO template (2×2 cm^2) and evenly spread across the surface. The AAO template was then spin-coated at 5000 rpm for 1 min. Finally, aluminum foil was placed on a hot plate preheated to 100 °C, and the AAO template loaded with the sample was placed on the aluminum foil and heated for 5 min to promote solvent evaporation and confined crystallization. This deposition and crystallization process was repeated ten times to obtain the $Cs_3Cu_2Br_{1.25}I_{3.75}$-AAO scintillation screen.

2.5. Performance Characterization Methods

X-ray diffraction (XRD) patterns were collected using a high-resolution X-ray diffractometer (D8 Discover, Bruker AXS GmbH, Karlsruhe, Germany)) with Cu Kα radiation (λ = 1.541 Å). Absorption spectra were measured using a Shimadzu UV-2700 UV-visible-near-infrared spectrophotometer (Shanghai, China). Photoluminescence (PL) and X-ray-excited radioluminescence (RL) spectra were recorded using a Zolix OmniFluo 960SP spectrometer (Beijing, China) equipped with an FLS-XrayV module. X-ray imaging performance was evaluated by recording images with a Fortune technologyFT-XW500 digital camera (Shenzhen, China).

3. Results and Discussion

Figure 1a illustrates the in situ growth process of $Cs_3Cu_2Br_{1.25}I_{3.75}$ crystals within the AAO template. In the experiment, a pre-prepared precursor solution was uniformly spread onto the AAO surface through multiple spin-coating cycles, while the infiltration of the solution into the nanopores was mainly driven by capillary forces. Subsequent thermal treatment promoted gradual crystallization and the oriented arrangement of the crystals inside the template channels. As shown in Figure 1b, ultraviolet fluorescence images reveal that the surface distribution uniformity of $Cs_3Cu_2Br_{1.25}I_{3.75}$ crystals on the AAO template visibly improves with increasing spin-coating cycles. To further verify the crystal structure of the obtained material, Figure 1c presents the X-ray diffraction (XRD) pattern of the $Cs_3Cu_2Br_{1.25}I_{3.75}$-AAO film. All diffraction peaks arising from the evaporation-assisted crystallization process are consistent with those of $Cs_3Cu_2Br_{1.25}I_{3.75}$ powder prepared by the cooling crystallization method. In addition, several extra diffraction peaks corresponding to Al_2O_3 are observed, indicating that $Cs_3Cu_2Br_{1.25}I_{3.75}$ perovskite crystals were successfully grown in situ within the AAO membrane. Figure 1d,e shows the crystal structure analysis, which demonstrates that $Cs_3Cu_2Br_{1.25}I_{3.75}$ and $Cs_3Cu_2Br_5$ possess similar crystal structures [31,32]. The Cu ions occupy two distinct coordination environments, namely tetrahedral and trigonal sites, forming two different structural units. These units are interconnected through the sharing of two halide ions, while Cs ions are located between the polyhedral units, separating the structural frameworks.

The X-ray absorption capability of a scintillator directly determines its detection efficiency and luminescence performance and is therefore considered one of the key parameters for evaluating scintillator materials [33]. By utilizing photon cross-section databases (the NIST XCOM database), we systematically compared the X-ray absorption properties of $Cs_3Cu_2Br_{1.25}I_{3.75}$ with those of commercially available scintillators, as shown in Figure 2a. The results indicate that $Cs_3Cu_2Br_{1.25}I_{3.75}$ exhibits absorption performance comparable to, or even competitive with, that of commercial scintillators such as CsI: Tl, BGO, and LYSO over the entire X-ray energy range. It is worth noting that the contribution of the Al substrate at the bottom of the AAO template to X-ray absorption is negligible, which was further confirmed by additional calculations.

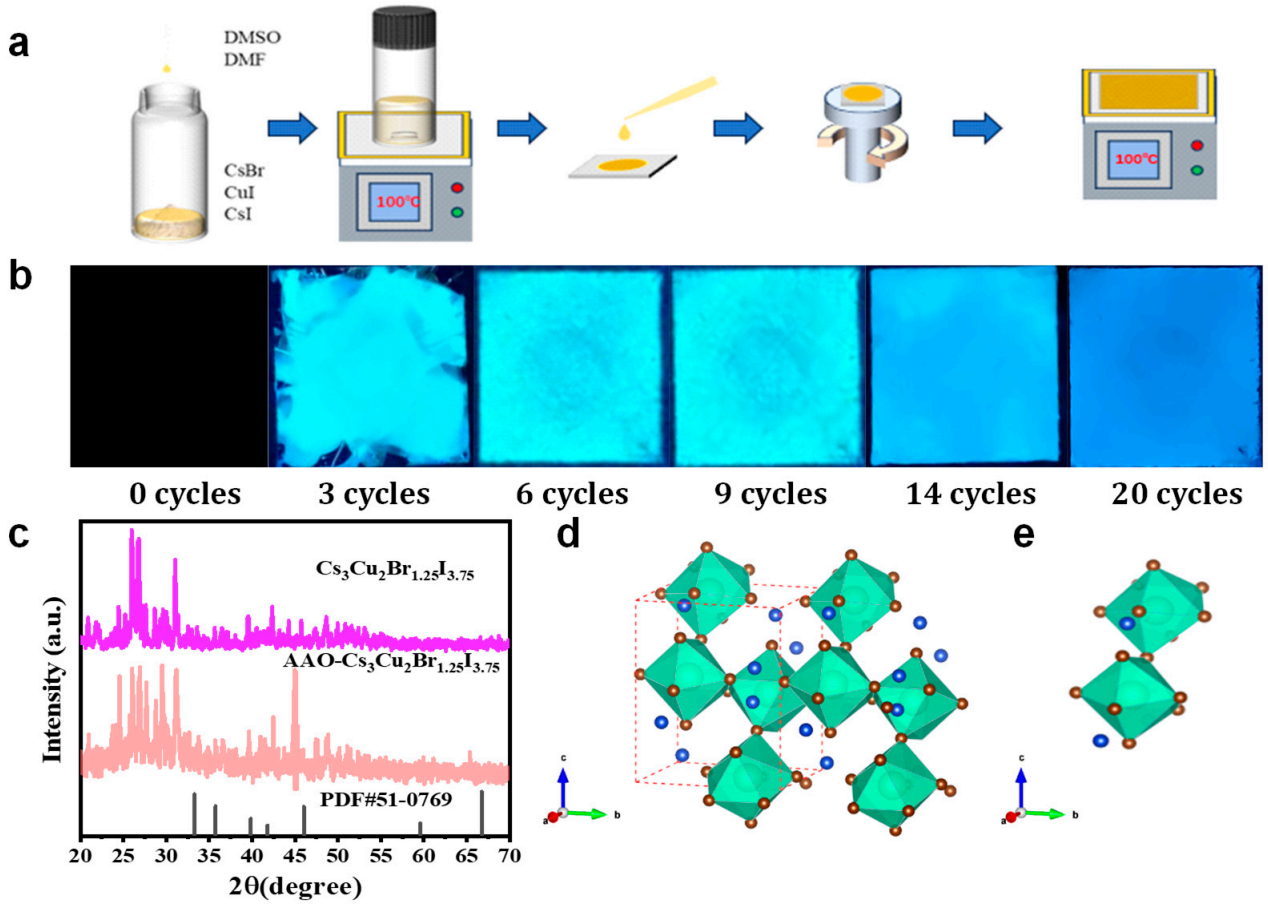

Figure 1. (**a**) In situ growth process of $Cs_3Cu_2Br_{1.25}I_{3.75}$ crystals within an anodic aluminum oxide (AAO) template; (**b**) Growth behavior of $Cs_3Cu_2Br_{1.25}I_{3.75}$ in the AAO template under different spin-coating cycles; (**c**) X-ray diffraction (XRD) pattern of the $Cs_3Cu_2Br_{1.25}I_{3.75}$-AAO film; (**d**) Crystal structure of $Cs_3Cu_2Br_{1.25}I_{3.75}$:Blue spheres represent Cs^+ cations, brown spheres denote disordered halogen sites occupied by Br^- and I^- ions, green polyhedra indicate the Cu^{2+} coordination environment, and the red dashed frame outlines a single unit cell; (**e**) $Cs_3Cu_2Br_{1.25}I_{3.75}$ smallest structural unit.

Furthermore, experimental measurements show that a $Cs_3Cu_2Br_{1.25}I_{3.75}$ sample with a thickness of 400 μm can effectively attenuate 50 keV X-rays, achieving nearly complete absorption of the incident radiation, as illustrated in Figure 2b. In contrast, an Al substrate with the same thickness exhibits much weaker attenuation capability, indicating that the presence of the Al substrate does not introduce a significant influence during practical imaging processes. Figure 2c presents the X-ray-excited radioluminescence (RL) spectra of the $Cs_3Cu_2Br_{1.25}I_{3.75}$-AAO film under different radiation dose rates. The integrated RL intensity as a function of dose rate was further extracted, as shown in Figure 2d. A good linear response is maintained even at a dose rate as low as 6 mGy/s, which excludes the contribution from defect-related emission. In addition, the minimum detectable dose rate of the $Cs_3Cu_2Br_{1.25}I_{3.75}$-AAO scintillator was evaluated. At a signal-to-noise ratio (SNR) of 3, the detection limit was determined to be 243 nGy/s, which is significantly lower than the typical dose rate (~5.5 μGy/s) required for medical X-ray diagnostic imaging, as reported in the literature [34].

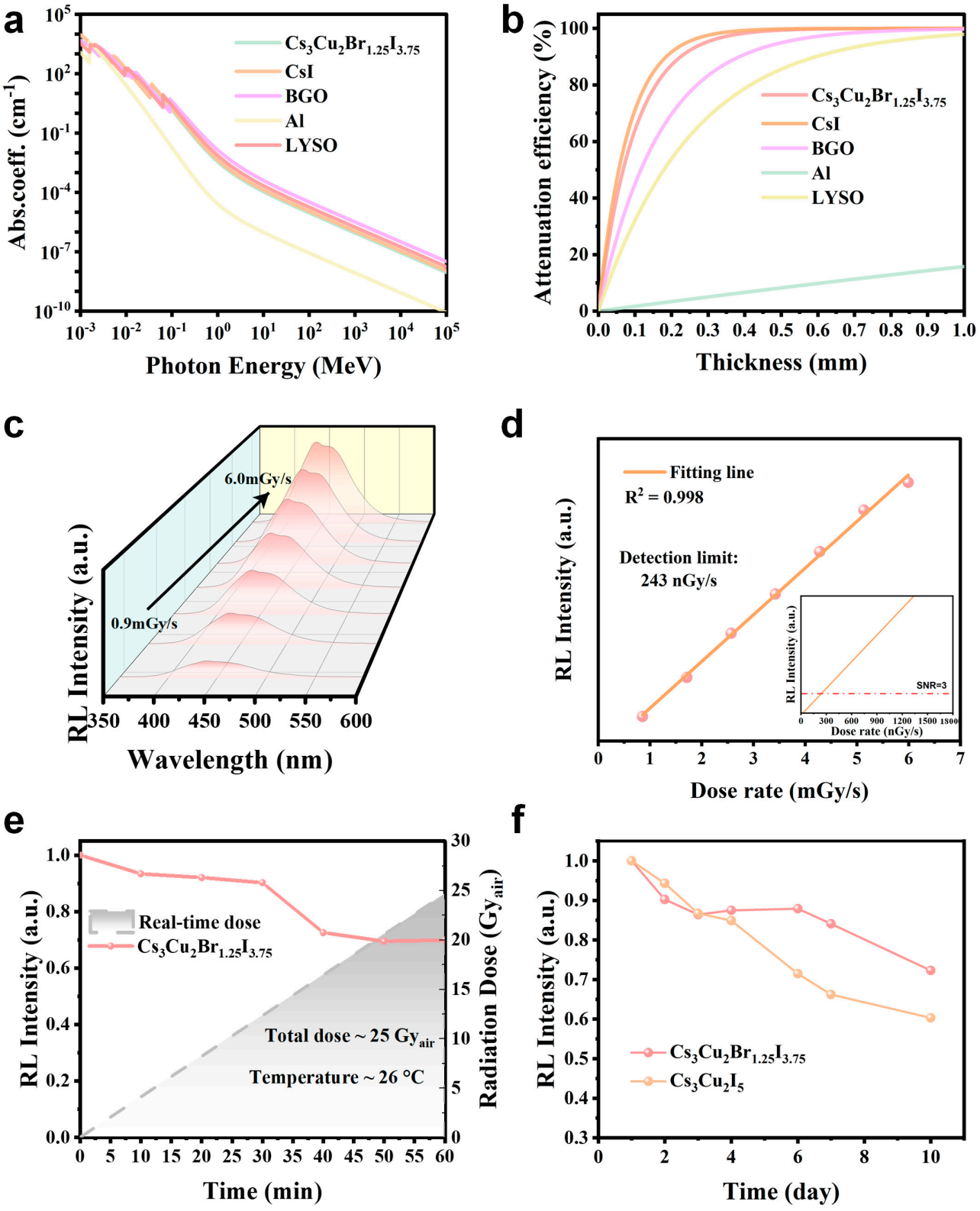

Figure 2. (**a**) Comparison of the X-ray absorption coefficients of $Cs_3Cu_2Br_{1.25}I_{3.75}$ and representative scintillator materials at different photon energies; (**b**) X-ray attenuation efficiency as a function of material thickness, calculated using linear attenuation coefficients at a photon energy of 50 keV, demonstrating the radiation shielding performance under this energy condition; (**c**) Radioluminescence (RL) intensity responses under different X-ray dose rates; (**d**) Linear relationship between RL intensity and dose rate (R^2 = 0.998), with a detection limit of 243 nGy/s (inset: linear fitting in the low-dose region); (**e**) RL stability under a total accumulated dose of approximately 25 Gy/air; (**f**) RL intensity for $Cs_3Cu_2Br_{1.25}I_{3.75}$-AAO and $Cs_3Cu_2I_5$ under ambient conditions over 10 days.

To comprehensively evaluate the practical application potential of $Cs_3Cu_2Br_{1.25}I_{3.75}$-AAO, its stability under continuous X-ray irradiation was systematically investigated. As shown in Figure 2e, the $Cs_3Cu_2Br_{1.25}I_{3.75}$-AAO composite exhibits excellent radiation tolerance under continuous exposure to 50 keV X-rays. After more than 1 h of irradiation, corresponding to a cumulative dose exceeding 25 Gy/air, the integrated RL intensity remains at approximately 70% of its initial value. These results demonstrate the reliability and durability of $Cs_3Cu_2Br_{1.25}I_{3.75}$-AAO in practical applications, particularly for imaging scenarios requiring sub-second exposure times, where the performance exceeds current application requirements [35]. Figure 2f shows the RL intensity evolution of the $Cs_3Cu_2Br_{1.25}I_{3.75}$-AAO material under ambient conditions over a period of 10 days. During one week of natural storage, the RL intensity remains above 70% of its initial value. In comparison, undoped $Cs_3Cu_2I_5$ single crystals exhibit a decrease to approximately 60% within one week [22], indicating that $Cs_3Cu_2Br_{1.25}I_{3.75}$-AAO displays superior RL stability.

Figure 3a shows the photoluminescence excitation (PLE) and photoluminescence (PL) spectra of the synthesized $Cs_3Cu_2Br_{1.25}I_{3.75}$-AAO. Under excitation at 307 nm, a bright blue emission peak centered at 437 nm is observed for $Cs_3Cu_2Br_{1.25}I_{3.75}$-AAO. The emission exhibits a full width at half maximum (FWHM) exceeding 90 nm and a large Stokes shift of approximately 130 nm, which is characteristic of self-trapped exciton (STE) emission. Notably, there is negligible spectral overlap between the excitation and emission spectra, indicating minimal self-absorption behavior. To further investigate the emission characteristics, PL spectra were recorded under different excitation wavelengths, and PLE spectra were collected at different emission wavelengths. As shown in Figure 3b,c, $Cs_3Cu_2Br_{1.25}I_{3.75}$-AAO was excited using wavelengths ranging from 280 to 320 nm, resulting in multiple PL spectra. After normalization, these PL spectra nearly overlap, exhibiting identical peak positions and spectral widths. This behavior indicates that the position and shape of the emission band remain unchanged as the excitation wavelength varies within the 280–320 nm excitation range. In addition, PLE spectra were recorded by monitoring emission wavelengths from 405 to 465 nm. After normalization, the PLE spectra also show nearly identical peak positions and bandwidths. Furthermore, as shown in Figure 3d, the normalized PL and radioluminescence (RL) spectra overlap well, suggesting that the excited charge carriers undergo a single radiative recombination pathway. This observation implies that the entire emission band originates from the same dynamic process. Unlike three-dimensional perovskite structures, these zero-dimensional structures based on isolated $[Cu_2X_5]^{3-}$ units exhibit strong electron-phonon coupling and pronounced exciton localization. Consequently, they give rise to broadband emission with a large Stokes shift induced by STEs. These features, including the broad emission bandwidth and large Stokes shift, are fully consistent with the spectral characteristics observed in this work.

Furthermore, the luminescence efficiency and emission dynamics of the $Cs_3Cu_2Br_{1.25}I_{3.75}$-AAO array were systematically characterized. As shown in Figure 3e, the absolute photoluminescence intensity was measured using an integrating sphere system with $BaSO_4$ as the reference material, and the corresponding photoluminescence quantum yield (PLQY) was determined to be 64%. This result indicates a high radiative efficiency during the excited-state recombination process and further confirms the effectiveness and dominant role of the self-trapped exciton (STE) radiative recombination pathway. Figure 3f presents the time-resolved photoluminescence decay curve under pulsed excitation. By fitting the decay profile with a single-exponential function, a photoluminescence lifetime (τ) of 1.93 μs was obtained, which is characteristic of microsecond-scale emission associated with STEs. Overall, $Cs_3Cu_2Br_{1.25}I_{3.75}$-AAO exhibits pronounced STE-dominated emission behavior, high quantum efficiency, and well-defined emission dynamics, thereby providing a solid foundation for its application in high-resolution, low-dose X-ray imaging.

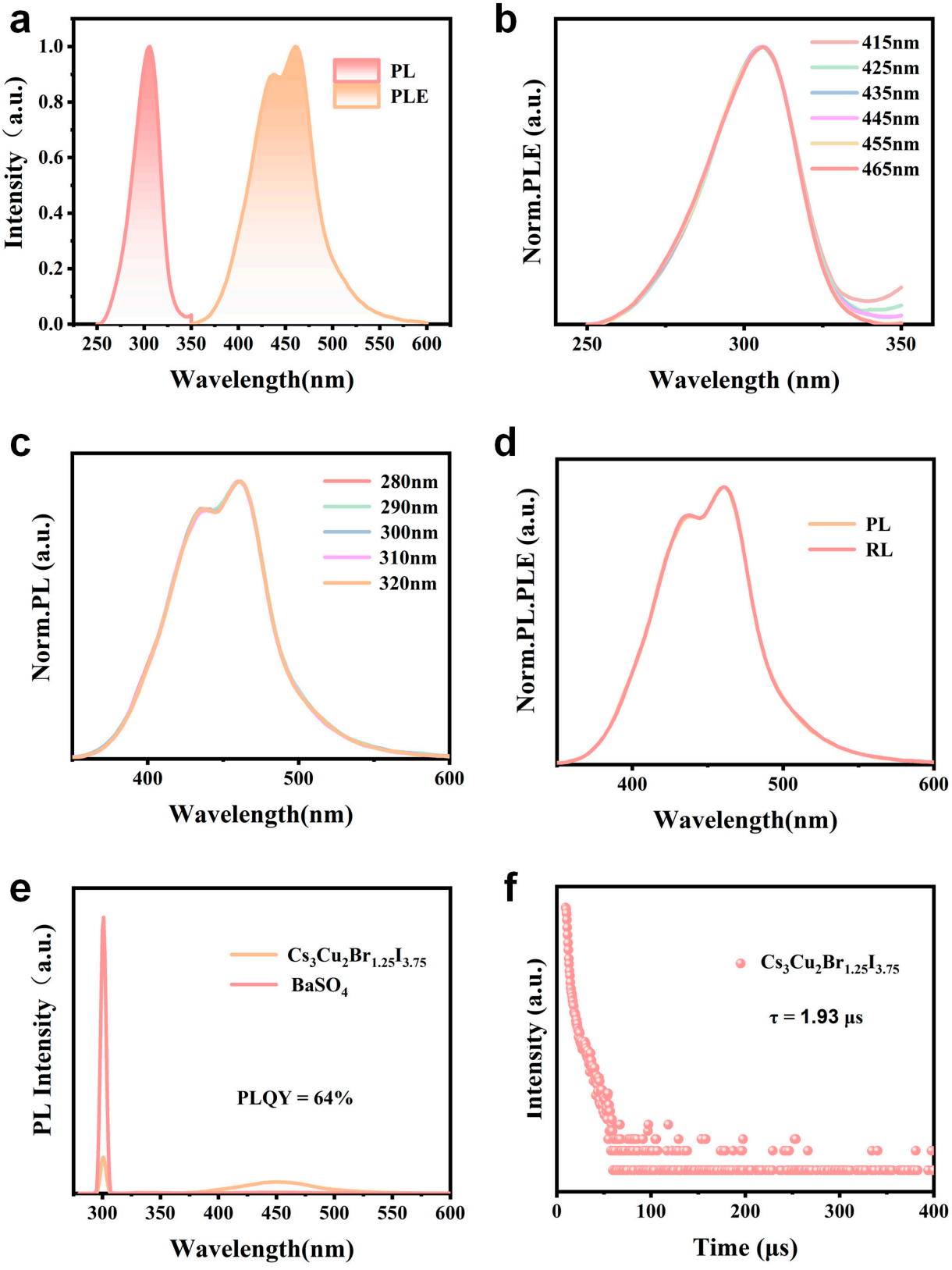

Figure 3. (**a**) Photoluminescence (PL) and photoluminescence excitation (PLE) spectra of $Cs_3Cu_2Br_{1.25}I_{3.75}$-AAO; (**b**) PLE spectra of $Cs_3Cu_2Br_{1.25}I_{3.75}$-AAO recorded at various emission wavelengths ranging from 405 to 465 nm; (**c**) PL spectra of $Cs_3Cu_2Br_{1.25}I_{3.75}$-AAO under excitation wavelengths from 280 to 320 nm; (**d**) Normalized PL and radioluminescence (RL) spectra of $Cs_3Cu_2Br_{1.25}I_{3.75}$-AAO; (**e**) Absolute photoluminescence intensity of $Cs_3Cu_2Br_{1.25}I_{3.75}$ measured using an integrating sphere system with $BaSO_4$ as the diffuse reflectance standard. (**f**) Time-resolved photoluminescence spectra of $Cs_3Cu_2Br_{1.25}I_{3.75}$-AAO.

Figure 4a,b show scanning electron microscopy (SEM) images of the pristine AAO template and the surface of the $Cs_3Cu_2Br_{1.25}I_{3.75}$-AAO array, respectively. It can be observed that, through the spatially confined evaporation-assisted crystallization process, the $Cs_3Cu_2Br_{1.25}I_{3.75}$ precursor solution enables successful in situ growth of arrayed nanocrystals within the AAO pores. The resulting arrays exhibit a regular arrangement and uniform pore size, indicating good reproducibility of the template-guided growth process. To evaluate the imaging performance, X-ray imaging experiments were carried out using a 35 keV X-ray source to irradiate test objects containing internal structures, and the scintillation images were recorded with a digital camera. The test objects included opaque capsules containing internal springs and 5 mm chips. Figure 4c presents photographs of representative test objects, such as the spring and the chip. Figure 4d,e display the X-ray images obtained using a conventional film-type $Cs_3Cu_2Br_{1.25}I_{3.75}$ scintillator ($Cs_3Cu_2Br_{1.25}I_{3.75}$-Film) and the array-structured $Cs_3Cu_2Br_{1.25}I_{3.75}$-AAO scintillator, respectively. Although both scintillators are capable of resolving the internal information of the test objects, a clear comparison reveals that the array-structured $Cs_3Cu_2Br_{1.25}I_{3.75}$-AAO produces images with higher clarity and sharper edges. The spatial resolution was first evaluated using images of a standard line-pair phantom, as shown in Figure 4f. The $Cs_3Cu_2Br_{1.25}I_{3.75}$-AAO scintillator achieves a spatial resolution of 11.10 lp/mm, representing a significant improvement compared with the resolution of 4.00 lp/mm obtained for the $Cs_3Cu_2Br_{1.25}I_{3.75}$-Film. Further quantitative analysis was performed using the standard slanted-edge method. As shown in Figure 4g, at a modulation transfer function (MTF) value of 0.2, the spatial resolutions of $Cs_3Cu_2Br_{1.25}I_{3.75}$-Film and $Cs_3Cu_2Br_{1.25}I_{3.75}$-AAO are determined to be 5.90 lp/mm and 14.10 lp/mm, respectively. These imaging results indicate that the AAO nanoporous array structure, by providing enhanced optical confinement and suppressing lateral scintillation photon spreading, plays a dominant role in improving spatial resolution and edge sharpness, rather than changes in the intrinsic scintillation properties of $Cs_3Cu_2Br_{1.25}I_{3.75}$ itself.

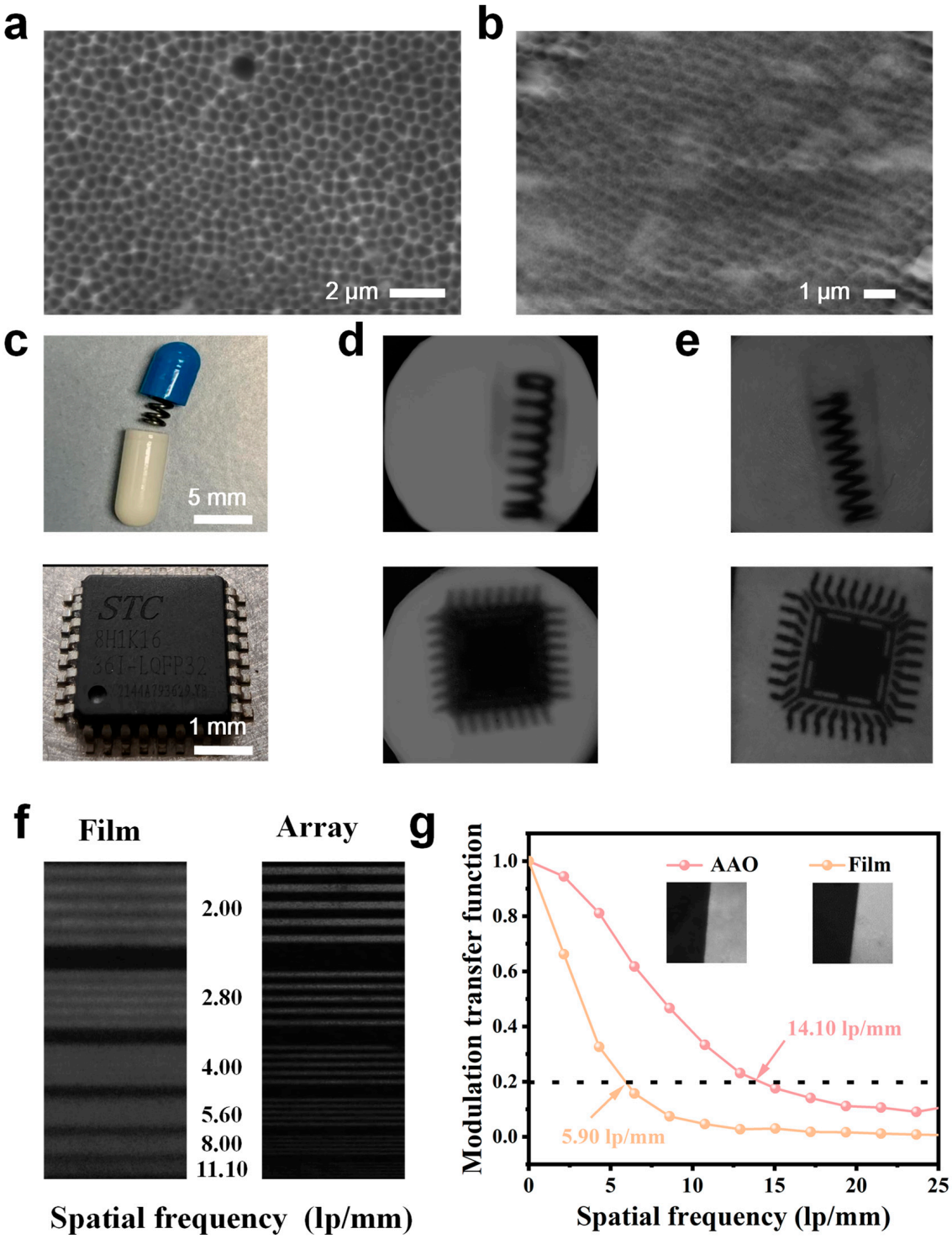

Figure 4. (**a**) SEM image of the surface of the pristine AAO template; (**b**) SEM image of the surface of the $Cs_3Cu_2Br_{1.25}I_{3.75}$-AAO scintillator; (**c**) Photographs of the test objects (spring and chip); (**d**) X-ray imaging result obtained using the $Cs_3Cu_2Br_{1.25}I_{3.75}$-Film scintillator; (**e**) X-ray imaging result obtained using the $Cs_3Cu_2Br_{1.25}I_{3.75}$-AAO scintillator; (**f**) Modulation transfer function (MTF) curve measured using the standard slanted-edge method for the $Cs_3Cu_2Br_{1.25}I_{3.75}$-Film scintillator; the inset shows the corresponding slanted-edge image and the imaging result of a standard X-ray resolution test card obtained with the $Cs_3Cu_2Br_{1.25}I_{3.75}$-AAO scintillator; (**g**) Modulation transfer function (MTF) curves of $Cs_3Cu_2Br_{1.25}I_{3.75}$-AAO and $Cs_3Cu_2Br_{1.25}I_{3.75}$-Film scintillators, where the black dashed line represents the MTF = 0.2 threshold for defining limiting spatial resolution (inset: corresponding slanted-edge image).

4. Conclusions

In this study, a spatially confined evaporation-assisted crystallization strategy was proposed and demonstrated to enable the in situ growth of $Cs_3Cu_2Br_{1.25}I_{3.75}$ nanoarray scintillators within anodic aluminum oxide (AAO) templates. Leveraging the high ordering, uniform pore dimensions, and good processability of the AAO template, $Cs_3Cu_2Br_{1.25}I_{3.75}$ was grown in an arrayed manner within nanoscale pores. The resulting arrayed scintillator exhibits a photoluminescence quantum yield of 62% and a microsecond-scale lifetime of 1.93 μs. The emission process is dominated by self-trapped excitons (STEs), characterized by a large Stokes shift and broadband emission, which is favorable for efficient radiative recombination and reduced optical crosstalk in imaging applications.

Under X-ray excitation, the $Cs_3Cu_2Br_{1.25}I_{3.75}$-AAO array demonstrates strong imaging performance, achieving a spatial resolution of 14.10 lp/mm and a low detection limit of 243 nGy/s, exceeding the performance reported for most lead-free perovskite-based scintillators. Compared with conventional thick-film $Cs_3Cu_2Br_{1.25}I_{3.75}$ scintillators, the arrayed structure shows clear advantages in image sharpness, contrast, and fine-detail resolution. These improvements are primarily attributed to the longitudinal optical waveguiding effect and lateral optical isolation between adjacent pixels provided by the AAO template, which effectively reduces lateral photon diffusion and signal crosstalk. In addition, the $Cs_3Cu_2Br_{1.25}I_{3.75}$-AAO scintillator exhibits good environmental and radiation stability, maintaining a high luminescence intensity under prolonged high-dose X-ray irradiation and during storage under ambient conditions. These results indicate its practical feasibility for real-world applications. Overall, the $Cs_3Cu_2Br_{1.25}I_{3.75}$-AAO array scintillator shows strong potential for high-resolution, low-dose X-ray imaging and provides a viable strategy for the development of cost-effective and structurally controllable scintillation screens.

Author Contributions: Conceptualization, X.L. and T.L.; methodology, X.L.; software, X.L., Z.Y. and B.Z.; validation, X.L., J.H. and Z.Z.; formal analysis, X.L.; investigation, X.L., Z.Y. and B.Z.; resources, T.L.; data curation, X.L., B.Z. and Z.Y.; writing—original draft preparation, X.L.; writing—review and editing, X.L. and T.L.; supervision, T.L.; project administration, T.L. All authors have read and agreed to the published version of the manuscript.

Funding: The Guangxi Natural Science Foundation (Nos. 2025GXNSFAA069543, 2025GXNSFAA069357) and the National Natural Science Foundation of China (No. 52472153).

Data Availability Statement: The original contributions presented in this study are included in the article. Further inquiries can be directed to the corresponding author.

Acknowledgments: During the preparation of this manuscript, the authors used ChatGPT (OpenAI, GPT-5.2) [M1.1] for language polishing and improvement of academic expression only. The scientific content, experimental design, data analysis, results, and conclusions were entirely developed and verified by the authors. The authors take full responsibility for the integrity and originality of this work.

Conflicts of Interest: The authors declare no conflicts of interest.

References

1. Ou, X.; Chen, X.; Xu, X.; Xie, L.; Chen, X.; Hong, Z.; Bai, H.; Liu, X.; Chen, Q.; Li, L.; et al. Recent Development in X-Ray Imaging Technology: Future and Challenges. *Research* **2021**, *2021*, 9892152. [CrossRef] [PubMed]
2. Pang, J.; Wu, H.; Li, H.; Jin, T.; Tang, J.; Niu, G. Reconfigurable perovskite X-ray detector for intelligent imaging. *Nat. Commun.* **2024**, *15*, 1769. [CrossRef]
3. Sakhatskyi, K.; Turedi, B.; Matt, G.J.; Wu, E.; Sakhatska, A.; Bartosh, V.; Lintangpradipto, M.N.; Naphade, R.; Shorubalko, I.; Mohammed, O.F.; et al. Stable perovskite single-crystal X-ray imaging detectors with single-photon sensitivity. *Nat. Photonics* **2023**, *17*, 510–517. [CrossRef]

4. Wang, J.-X.; Shekhah, O.; Bakr, O.M.; Eddaoudi, M.; Mohammed, O.F. Energy transfer-based X-ray imaging scintillators. *Chem* **2025**, *11*, 102273. [CrossRef]
5. Li, H.; Wang, C.-f.; Luo, Q.-f.; Ma, C.; Zhang, J.; Zhao, R.; Yang, T.; Du, Y.; Chen, X.; Li, T.; et al. Wearable Photoferroelectric Perovskite X-Ray Detectors. *Adv. Funct. Mater.* **2024**, *34*, 2407693. [CrossRef]
6. Spahn, M. X-ray detectors in medical imaging. *Nucl. Instrum. Methods Phys. Res. Sect. A Accel. Spectrometers Detect. Assoc. Equip.* **2013**, *731*, 57–63. [CrossRef]
7. Zentai, G.; Partain, L.; Pavlyuchkova, R.; Proano, C.; Schieber, M.; Shah, K.; Bennett, P. Comparison of mercuric iodide and lead iodide X-ray detectors for X-ray imaging applications. In Proceedings of the Nuclear Science Symposium/Medical Imaging Conference, Rome, Italy, 16–22 October 2004; pp. 2278–2282.
8. Cha, B.K.; Jeon, S.; Lee, M.; Lee, H.; Cho, H.; Seo, C.W. Design and performance evaluation of different high-resolution scintillators in digital X-ray imaging detector. *Nucl. Instrum. Methods Phys. Res. Sect. A Accel. Spectrometers Detect. Assoc. Equip.* **2024**, *1063*, 169323. [CrossRef]
9. He, G.L.; Li, L.J.; Chen, J.Y.; Gong, Y.J.; Guo, H. An efficient Cu^{+} doped Gd-based fluoroaluminosilicate scintillator glass for X-ray detectors. *J. Mater. Chem. C* **2025**, *13*, 1325–1331. [CrossRef]
10. Wu, Z.; Jia, W.; Wu, Y.; Hei, D.; Sun, A.; Ling, Y.; Shan, Q.; Shi, C.; Zhang, J. Design of a five-layers multi-energy X-ray imaging detector for material sorting. *Appl. Radiat. Isot.* **2023**, *194*, 110711. [CrossRef] [PubMed]
11. Yang, L.; Li, Z.; He, L.; Sun, J.; Wang, J.; Wang, Y.; Li, M.; Zhu, Z.; Dai, X.; Hu, S.; et al. Emergence of a Lanthanide Chalcogenide as an Ideal Scintillator for a Flexible X-ray Detector. *Angew. Chem. Int. Ed.* **2023**, *62*, e202306465. [CrossRef] [PubMed]
12. Zhang, Q.; Zhang, S.; Zheng, R.; Du, P.; Ding, J.; Wei, W. High-efficiency narrow-band green-emitting Tb-doped fluorosilicate glass for X-ray detectors. *J. Non Cryst. Solids* **2023**, *608*, 122236. [CrossRef]
13. Han, M.; Xiao, Y.; Zhou, C.; Yang, Y.; Wu, X.; Hu, Q.; Jin, X.; Zhang, W.; Hu, J.-S.; Jiang, Y. Recent advances on two-dimensional metal halide perovskite x-ray detectors. *Mater. Futures* **2023**, *2*, 012104. [CrossRef]
14. Wang, B.; Yang, X.; Li, R.; Qaid, S.M.H.; Cai, W.; Xiao, H.; Zang, Z. One-Dimensional $CsCu_2I_3$ Single-Crystal X-ray Detectors. *ACS Energy Lett.* **2023**, *8*, 4406–4413. [CrossRef]
15. Wang, W.; Cai, M.; Liu, X.; Ji, K.; Yu, X.; Dai, S. Metal halide perovskite single crystal growth and application for X-ray detectors. *J. Mater. Chem. C* **2023**, *11*, 12105–12127. [CrossRef]
16. Hao, X.; Nie, L.; Zhu, X.; Zeng, G.; Liu, C.; Teng, Z.; Liu, H.; Yue, Y.; Yu, X.; Wang, T. High-Resolution X-ray Image from Copper-Based Perovskite Hybrid Polymer. *ACS Appl. Mater. Interfaces* **2024**, *16*, 29210–29216. [CrossRef]
17. Zhou, W.; Zhu, X.; Yu, J.; Mou, D.; Li, H.; Kong, L.; Lang, T.; Peng, L.; Chen, W.; Xu, X.; et al. High-Quality $Cs_3Cu_2I_5$@PMMA Scintillator Films Assisted by Multiprocessing for X-ray Imaging. *ACS Appl. Mater. Interfaces* **2023**, *15*, 38741–38749. [CrossRef]
18. Han, L.; Zhao, J.; Miao, Y.; Zhou, W.; Yuan, M.; Cui, J.; Ci, Z. Thermal stability and flexible X-Ray scintillation screen through in-situ assembling $Cs_3Cu_2Cl_5$ nanocrystals in polymer matrix. *Mater. Res. Bull.* **2024**, *179*, 112980. [CrossRef]
19. Xiang, W.; Shen, D.; Zhang, X.; Li, X.; Liu, Y.; Zhang, Y. Transparent and Planar $C_{s3}Cu_2Cl_5$ Crystals for Micrometer-Resolution X-ray Imaging Screen. *ACS Appl. Mater. Interfaces* **2024**, *16*, 4918–4924. [CrossRef]
20. Roccanova, R.; Yangui, A.; Nhalil, H.; Shi, H.; Du, M.-H.; Saparov, B. Near-Unity Photoluminescence Quantum Yield in Blue-Emitting $Cs_3Cu_2Br_{5-x}I_x$ ($0 \leq x \leq 5$). *ACS Appl. Electron. Mater.* **2019**, *1*, 269–274. [CrossRef]
21. Ren, Y.; Lü, S. Industrial mass production of novel mixed-halide $Cs_3Cu_2Cl_{5-x}I_x$ and $Cs_5Cu_3Cl_{8-x}I_x$ compounds with greatly enhanced stability and luminescent efficiency by compositional engineering. *Chem. Eng. J.* **2021**, *417*, 129223. [CrossRef]
22. Liu, J.; Li, X.; Zhao, J.; Liu, H.; Lin, T. Efficient and stable $Cs_5Cu_3Cl_{8-x}I_x$ (x = 1,2) single crystalline scintillators for X-ray imaging. *J. Alloys Compd.* **2025**, *1021*, 179659. [CrossRef]
23. Zhao, B.-Z.; Qin, X.-B.; Feng, Z.-D.; Wei, C.-F.; Chen, Y.; Wang, B.-Y.; Wei, L. Performance evaluation of CsI screens for X-ray imaging. *Chin. Phys. C* **2014**, *38*, 116003. [CrossRef]
24. Rocha, J.G.; Dias, R.A.; Goncalves, L.; Minas, G.; Ferreira, A.; Costa, C.M.; Lanceros-Mendez, S. X-Ray Image Detector Based on Light Guides and Scintillators. *IEEE Sens. J.* **2009**, *9*, 1154–1159. [CrossRef]
25. Cha, B.K.; Kim, J.Y.; Cho, G.; Seo, C.-W.; Jeon, S.; Huh, Y. Quasi-pixel structured nanocrystalline Gd_2O_3 (Eu) scintillation screens and imaging performance for indirect X-ray imaging sensors. *Nucl. Instrum. Methods Phys. Res. Sect. A Accel. Spectrometers Detect. Assoc. Equip.* **2011**, *648*, S12–S15. [CrossRef]
26. Shao, W.; He, T.; Wang, L.; Wang, J.-X.; Zhou, Y.; Shao, B.; Ugur, E.; Wu, W.; Zhang, Z.; Liang, H.; et al. Capillary Manganese Halide Needle-Like Array Scintillator with Isolated Light Crosstalk for Micro-X-Ray Imaging. *Adv. Mater.* **2024**, *36*, 2312053. [CrossRef]
27. Wang, S.; Gu, Z.; Zhao, R.; Zhang, T.; Lou, Y.; Guo, L.; Su, M.; Li, L.; Zhang, Y.; Song, Y. A general method for growth of perovskite single-crystal arrays for high performance photodetectors. *Nano Res.* **2022**, *15*, 6568–6573. [CrossRef]
28. Hui, J.; Ran, P.; Su, Y.; Yang, L.; Xu, X.; Liu, T.; Yang, Y.M. High-Resolution X-ray Imaging Based on Solution-Phase-Synthesized $Cs_3Cu_2I_5$ Scintillator Nanowire Array. *J. Phys. Chem. C* **2022**, *126*, 12882–12888. [CrossRef]

29. Liang, D.; Tan, L.; Lu, S.; Sun, Z.; Wang, H.; Cai, W.; Zang, Z. Low-Temperature Solution Synthesis of Stable $Cs_3Cu_2Br_5$ Single Crystals for Visible Light Communications. *ACS Appl Mater Interfaces* **2023**, *15*, 24622–24628. [CrossRef]
30. Jun, T.; Sim, K.; Iimura, S.; Sasase, M.; Kamioka, H.; Kim, J.; Hosono, H. Lead-Free Highly Efficient Blue-Emitting $Cs_3Cu_2I_5$ with 0D Electronic Structure. *Adv. Mater.* **2018**, *30*, 1804547. [CrossRef]
31. Zeng, B.; Liu, Y.; Bao, S.; Wang, C.; Xu, R.; Liu, J.; Zhu, Y. The growth of $Cs_3Cu_2Br_5$ and $CsCu_2Br_3$ single crystals by cooling crystallization for scintillator application. *Crystengcomm* **2025**, *27*, 2888–2894. [CrossRef]
32. Zheng, X.; Huang, J.; Liu, Y.; Wang, T.; Han, S.; Wang, Z.; Teng, B.; Ji, S. Stable Lead-Free Blue-Emitting $Cs_3Cu_2Br_5$ Single Crystal with Self-Trap Exciton Emission for Optoelectronics. *Adv. Photonics Res.* **2022**, *3*, 2100289. [CrossRef]
33. Yanagida, T. Inorganic scintillating materials and scintillation detectors. *Proc. Jpn. Acad. Ser. B* **2018**, *94*, 75–97. [CrossRef] [PubMed]
34. Clairand, I.; Bordy, J.M.; Carinou, E.; Daures, J.; Debroas, J.; Denozière, M.; Donadille, L.; Ginjaume, M.; Itié, C.; Koukorava, C.; et al. Use of active personal dosemeters in interventional radiology and cardiology: Tests in laboratory conditions and recommendations—ORAMED project. *Radiat. Meas.* **2011**, *46*, 1252–1257. [CrossRef]
35. Yanagida, T.; Kato, T.; Nakauchi, D.; Kawaguchi, N. Fundamental aspects, recent progress and future prospects of inorganic scintillators. *Jpn. J. Appl. Phys.* **2023**, *62*, 010508. [CrossRef]